Research Article | Vol. 10, No. 1 | 1 Jan 2019 | BIOMEDICAL OPTICS EXPRESS 372

Biomedical Optics EXPRESS

Time domain X-ray luminescence computed tomography: numerical simulations

WEI ZHANG,[1] IGNACIO O. ROMERO,[2] AND CHANGQING LI[2,*]

[1]*Institute of Biomedical Engineering, Chinese Academy of Medical Science & Peking Union Medical College, Tianjin 300192, China*
[2]*Department of Bioengineering, University of California, Merced, Merced, CA 95343, USA*
[*]*cli32@ucmerced.edu*

Abstract: X-ray luminescence computed tomography (XLCT) has the potential to image the biodistribution of nanoparticles inside deep tissues. In XLCT, X-ray excitable nanophosphors emit optical photons for tomographic imaging. The lifetime of the nanophosphor signal, rather than its intensity, could be used to extract biological microenvironment information such as oxygenation in deep tumors. In this study, we propose the design, the forward model, and the reconstruction algorithm of a time domain XLCT for lifetime imaging with high spatial resolution. We have investigated the feasibility of the proposed design with numerical simulations. We found that the reconstructed lifetime images are robust to noise levels up to 5% and to unknown optical properties up to 4 times of absorption and scattering coefficients.

© 2018 Optical Society of America under the terms of the OSA Open Access Publishing Agreement

1. Introduction

X-ray luminescence computed tomography (XLCT) is an emerging hybrid imaging modality, in which high energy X-ray photons are used to excite X-ray excitable nanophosphors which emit optical photons measured for optical tomographic imaging [1]. The XLCT imaging is an intrinsic optical imaging with high measurement sensitivity and uses the known X-ray excitation region as anatomical guidance for high spatial resolution when imaging deep targets inside tissues [2,3]. So far, several XLCT systems have been proposed and validated with numerical simulations and experimental studies [4–7]. Currently, all XLCT systems work in a mode of continuous sampling, in which continuous-wave (CW) X-ray photons are used to excite fluorophores and the emitted optical intensity data is acquired for image reconstruction. Therefore, these CW XLCT systems do not have the ability for lifetime imaging which is related to many micro-environmental parameters such as oxygen concentration, temperature and pH value, etc.

Up to now, many different techniques including time domain (TD) and frequency domain (FD) solutions have been well developed to measure fluorescent lifetimes [8–10]. Although fast FD optical imaging systems have been commercially available, TD imaging methods, especially the time-correlated single photon counting (TCSPC) technique, which has better timing resolution, is considered to be the gold standard for high precision fluorescence lifetime imaging, due to its measurement accuracy [11,12]. Although the lifetime is independent of the depth, the spatial resolution of TD fluorescence imaging is also degraded by the strong optical scattering when imaging deep targets.

While similar to fluorescence lifetime imaging, phosphorescence lifetime imaging exhibits long luminescent lifetimes greater than fluorescent lifetimes due to their long-lived excited triplet states. Combined with time gating techniques, acquisition of these long emission lifetimes eliminates background fluorescence noise and overall improves the signal-to-noise ratio (SNR) of the phosphorescent lifetime signal [13]. Lifetime information serves as probe for detection and visualization of biomolecules in tissue [14]; analysis of the lifetime signal with fractional calculus establishes correlations between the lifetime of the excited nanophosphor and the biomolecule. For example, phosphorescent lifetimes are sensitive to

#347917 https://doi.org/10.1364/BOE.10.000372
Journal © 2019 Received 11 Oct 2018; revised 22 Nov 2018; accepted 26 Nov 2018; published 21 Dec 2018

Biomedical Optics EXPRESS

oxygen levels [13]; the long-lived excited state of the nanophosphor provides enough time for collisional interactions to occur between the nanophosphor and oxygen thus decreasing the lifetime. Oxygen concentrations are vital for radiation therapy since tumors in a hypoxic state become unresponsive to radiation treatment. Monitoring oxygen levels of tumors before and during therapy could improve radiation treatment results. Other applications of lifetime imaging allow for quantitative measurements of zinc, calcium and pH in cells [15,16]. Zinc is responsible for proper functioning and folding of proteins and are cofactors of viral proteins [17]. Calcium plays a significant role in signal transduction pathways and measurements of calcium in tissue could further advance studies in diseases such as Alzheimer's disease [18]. Homeostasis of pH is critical for regular cell metabolic functionalities, and lifetime imaging could record pH level fluctuations due to environmental changes within the cell [19]. The proposed time domain XLCT (tdXLCT) system has the potential to provide luminescent lifetime information of these biomolecules with high spatial resolution and sensitivity.

In this paper, we present a fiber-based tdXLCT system design in which we use pulsed, superfine X-ray beams to excite phosphors, and time resolved optical signals are detected by a photomultiplier tube (PMT) coupled to a TCSPC unit. The superfine X-ray beams, used as anatomical guidance in the time domain XLCT reconstruction, make it possible to have high spatial resolution lifetime imaging. The feasibility of this design is demonstrated through numerical simulations.

The paper is organized as follows. In section 2, we present the method, including the time domain XLCT imaging system design, the forward model, the reconstruction algorithms, numerical simulation setup, and the imaging evaluation criteria. Then, we present the numerical simulation results in section 3. Finally, we conclude the paper with some discussions in section 4.

2. Methods

2.1 Time domain XLCT system

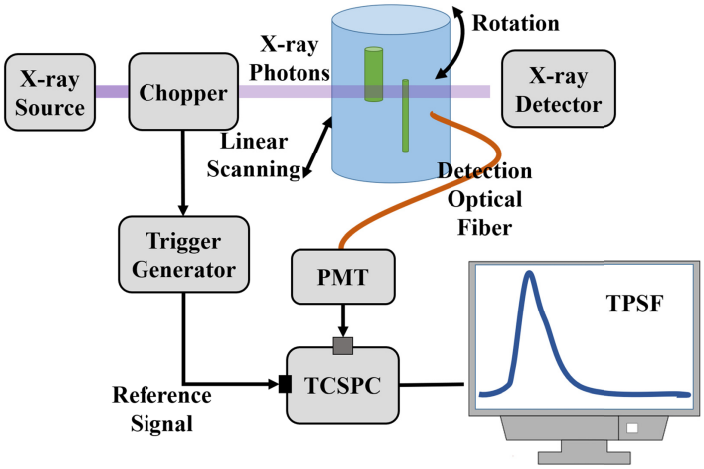

Fig. 1. Schematic of the proposed time domain XLCT system.

The schematic of the proposed time domain XLCT imaging system is plotted in Fig. 1. A focused X-ray tube (Polycapillary X-Beam Powerflux, XOS, New York; target metal: molybdenum (Mo)) is utilized to generate X-ray photons. A chopper system, $49.2\times49.2\,\mathrm{mm}^2$ which is similar to an optical chopper (MC2000B, Thorlabs, USA), chops the focused X-ray beam with a chopping frequency about 1 kHz. With the focusing X-ray beam diameter less than 100 micrometers, the X-ray pulse width is expected to be less than 1 microsecond. Meanwhile, the synchronous signal of the chopper system is acquired by a trigger generator

Biomedical Optics EXPRESS

and serves as the reference signal for the TCSPC device (SPC-130, Becker & Hickl, Germany). Phantoms or other objects for imaging are placed on a motorized rotation stage (B4872TS-ZR, Velmex, Inc., New York), which is mounted on a motorized linear stage (MB2509Q1J-S3, Velmex, Inc., New York). The scanning X-ray beam pass through objects and is then detected by an X-ray detector (Shad-o-Box 1024, GOS scintillator screen, Rad-icon Imaging Corp., California) with a detection area of consisting of a 1024×1024 pixel photodiode array sensor with a 48 μm pixel size. The X-ray detector measures the intensity of the X-ray beam, from which the phantom boundary is detected. The emitted optical photons from the phantom side surface are collected by a 2 meters long fiber bundle with an aperture diameter of 3 mm. The fiber bundle is fixed by a mount frame that moves and rotates with the phantom or the object being scanned. A fan-cooled photomultiplier tube (PMT) photon counting head (PMC-100, Becker & Hickl, Germany) is coupled to the TCSPC module for acquiring the time-resolved flux, *i.e.*, the temporal point spread function (TPSF). The measurement data is stored and displayed in a personal computer (PC).

2.2 Laplace transform based time domain XLCT algorithm

In this paper, we apply the generalized pulse spectrum technique (GPST) method to convert the real domain optical diffusion forward model into its Laplace transform, following the similar approach described in Ref [20]. for time domain fluorescence molecular tomography (FMT). In time domain XLCT, let $\Phi(\boldsymbol{r},p)=\int_0^{+\infty}\Phi(\boldsymbol{r},t)e^{-pt}dt$ be the Laplace transform of the time-dependent photon density $\Phi(\boldsymbol{r},t)$ at position $\boldsymbol{r}$ in domain Ω at time t for a complex transform factor p. The Laplace-transformed photon diffusion equation is accordingly written by the following equation:

$$\begin{cases}[\nabla\cdot D(\boldsymbol{r})\nabla-\mu_a(\boldsymbol{r})c-p]\Phi(\boldsymbol{r},p)=-S_k(\boldsymbol{r},p), & \boldsymbol{r}\in\Omega\\ c\Phi(\boldsymbol{r},p)+2KD(\boldsymbol{r})e_n\cdot\nabla\Phi(\boldsymbol{r},p)=0, & \boldsymbol{r}\in\partial\Omega\end{cases}\tag{1}$$

where $\mu_a(\boldsymbol{r})$ is the absorption coefficient of the media, c is the velocity of light in the media, $D(\boldsymbol{r})=[3(\mu_a(\boldsymbol{r})+\mu'_s(\boldsymbol{r}))]^{-1}$ is the diffusion coefficient, $\mu'_s(\boldsymbol{r})$ is the reduced scattering coefficient, $\boldsymbol{e}_n$ is the outward unity vector normal to the surface $\partial\Omega$, $K=(1+R_f)/(1-R_f)$ is the Robin boundary condition coefficient, R_f is the internal reflection coefficient at the boundary, and ∇ is the gradient coefficient. $S_k(\boldsymbol{r},p)$ is the source term which stands for the k-th X-ray beam illumination pattern and can be written as:

$$S_k(\boldsymbol{r},p)=T_k(\boldsymbol{r})\frac{\eta\mu_{af}(\boldsymbol{r})}{1+p\tau(\boldsymbol{r})}\tag{2}$$

where $T_k(\boldsymbol{r})$ is the X-ray intensity distribution, η is the quantum efficiency, and $\mu_{af}(\boldsymbol{r})$ is the absorption coefficient. In Eq. (2), the light yield $\eta\mu_{af}(\boldsymbol{r})$ and the lifetime $\tau(\boldsymbol{r})$ are the phosphorescent nanoparticle properties to be reconstructed.

In XLCT, while an X-ray beam scans the object along a straight line, the X-ray beam intensity distribution along the scanning line follows the Beer-Lambert law. If we assume a uniform X-ray attenuation medium, $T_k(\boldsymbol{r})$ can be expressed as:

$$T_k(r)=T_0\exp(-\mu_x(\boldsymbol{r})\times L(\boldsymbol{r}))\tag{3}$$

where T_0 is the initial X-ray beam intensity, $\mu_x(\boldsymbol{r})$ is the X-ray attenuation coefficient at the position $\boldsymbol{r}$, and $L(\boldsymbol{r})$ is the distance from X-ray beam start position to current position $\boldsymbol{r}$.

Biomedical Optics EXPRESS

Based on the finite element method (FEM), the forward model of the time domain XLCT can be expressed as [21]:

$$\mathbf{A}_{n_d \times I \times J, m}(p)\, \mathbf{x}_{m,1}(p) = \mathbf{b}_{n_d \times I \times J, 1}(p) \tag{4}$$

where n_d is the number of detector nodes, I is the total number of angular projections, J is the number of linear scan for each projection, and m is the finite element mesh node number. Here, we define the intermediate quantity, $x(\boldsymbol{r}, p) = \eta \mu_{af}(\boldsymbol{r}) / [1 + p\tau(\boldsymbol{r})]$. Let $x(\boldsymbol{r}, p) \approx \sum_{n=1}^{m} x_n(p)\, u_n(\boldsymbol{r}) = \mathbf{x}^T(p)\, \mathbf{u}(\boldsymbol{r})$ with $\mathbf{u}(\boldsymbol{r}) = [u_1(\boldsymbol{r}), u_2(\boldsymbol{r}), \ldots, u_m(\boldsymbol{r})]^T$ and $\mathbf{x}(p) = [x_1(p), x_2(p), \ldots, x_m(p)]^T$ being the shape functions and the unknowns. **b** is the measurement, and **A** is the system matrix that can be calculated as:

$$\mathbf{A}_{n_d \times I \times J, m}(p) = \begin{bmatrix} \begin{bmatrix} \Phi_1(p) \\ \vdots \\ \Phi_{n_d}(p) \end{bmatrix} \otimes \Gamma_1 \otimes T_1 \\ \vdots \\ \begin{bmatrix} \Phi_1(p) \\ \vdots \\ \Phi_{n_d}(p) \end{bmatrix} \otimes \Gamma_{I \times J} \otimes T_{I \times J} \end{bmatrix} \tag{5}$$

in which $\otimes$ is the element product of row vectors Φ_i , Γ_j and T_j , where $i \in [1, n_d]$ and $j \in [1, I \times J]$. $[\Phi_1(p), \Phi_2(p), \ldots, \Phi_{n_d}(p)]^T$ is the sensitivity matrix where each row vector Φ_i is solved by Eq. (1) when setting the detector node i to be 1. T_j is the excitation vectors from X-ray beam illumination patterns. In XLCT, the excitation regions have the known locations along the X-ray beam and can be described as:

$$\Gamma_j(s) = \begin{cases} 1, & \textit{node s is within the X-ray beam} \\ 0, & \textit{otherwise} \end{cases} \tag{6}$$

The XLCT reconstruction can be solved like what used in FMT [22–24]. The solution of Eq. (4) can be obtained by minimizing the following regularized squared measurement misfit under the non-negativity constraint:

$$\mathbf{x}(p) = \underset{\mathbf{x} \geq \mathbf{0}}{\mathbf{argmin}}\, \mathrm{F}(\mathbf{x}(p)) := \frac{1}{2} \| \mathbf{b}(p) - \mathbf{A}(p)\mathbf{x}(p) \|_2^2 + \alpha \| \mathbf{x}(p) \|_q^q \tag{7}$$

where α is the regularization parameter and $\| \mathbf{x}(p) \|_q^q$ $(q \geq 0)$ is the L^q norm term. In this paper, the majorization-minimization (MM) algorithm is applied to minimize the L^1 regularized mismatch between the measurements and the modeled values by updating the images iteratively. The details of the MM algorithm have been described elsewhere [23,24].

The two unknown distributions, the phosphorescent yield and the lifetime of the phosphor particles can be explicitly recovered from the images of $x(\boldsymbol{r}, p_1)$ and $x(\boldsymbol{r}, p_2)$ by employing a pair of transform factors: $p_{1,2}$, in the Laplace transforms:

Biomedical Optics EXPRESS

$$\begin{cases} \eta\mu_{af}(\boldsymbol{r}) = \dfrac{(p_1 - p_2)x(\boldsymbol{r}, p_1)x(\boldsymbol{r}, p_2)}{p_1 x(\boldsymbol{r}, p_1) - p_2 x(\boldsymbol{r}, p_2)} \\ \tau(\boldsymbol{r}) = -\dfrac{x(\boldsymbol{r}, p_1) - x(\boldsymbol{r}, p_1)}{p_1 x(\boldsymbol{r}, p_1) - p_2 x(\boldsymbol{r}, p_2)} \end{cases} \tag{8}$$

where the transform factors are:

$$p_{1,2} = \pm \frac{k}{(2/\mu_a^{(B)} c) + \tau^{(B)}}, \quad (0 \le k \le 1) \tag{9}$$

In which, $\mu_a^{(B)}$ and $\tau^{(B)}$ are the background optical absorption and lifetime coefficients. The transform factors p_1 and p_2 are two specific transform factors of p as defined in Eq. (8). In this study, we use a pair of transform factors only.

2.3 Numerical simulation studies

To validate our proposed time domain XLCT imaging system and algorithms, we have performed numerical simulation cases using a three-target phantom. To simulate the proposed imaging system, we took measurements using one optical fiber bundle. For the simulation studies, we used a 10 mm long cylindrical phantom with a diameter of 13 mm. The optical properties of the phantom were set to be $\mu_a^{(B)} = 0.0072\ mm^{-1}$ and $\mu'^{(B)}_s = 0.72\ mm^{-1}$, while, the phosphorescent properties were $\eta\mu_{af}^{(B)} = 0.001\ mm^{-1}$ and $\tau^{(B)} = 1\ ps$.

In numerical simulations, we adopted a normalized X-ray beam intensity. Therefore, the X-ray intensity at the entry to the phantom (T_0) was assumed to be equal to 1. The X-ray attenuation coefficient was $\mu_x = 0.0214\ mm^{-1}$ in the phantom. Then, the X-ray intensity along the X-ray beam in the phantom is given by the following equation:

$$T_k(\boldsymbol{r}) = \exp(-0.0214 \times L(\boldsymbol{r})) \tag{10}$$

where $L \in [0, 13]$ was the distance from one side to another side of the phantom.

All the three-targets had a diameter of 0.4 mm and a height of 6 mm and were embedded in the phantom. The positions of the targets are shown in Fig. 2, in which we can see that the target center-to-center distance (CtCD) was 0.8 mm. For numerical study, we set the phosphor particle concentration to be 1 mg/mL in targets and 0 mg/mL (no phosphors) in the background. Targets are divided in two groups: Group #1 including T1 and T2; Group #2 including T3.

Table 1. Optical and phosphorescent parameters of the phantom and targets

Items	μ_a [mm^{-1}]	μ'_s [mm^{-1}]	$\eta\mu_{af}$ [mm^{-1}]	τ [ps]
Background	0.0072	0.72	0.001	1
Group 1	0.0072	0.72	0.005	400
Group 2	0.0072	0.72	0.003	600

The fiber bundle was placed at 3 mm under the phantom top surface. The relative position of fiber bundle to the phantom was fixed. During the experiments, the fiber bundle and the phantom translated and rotated together. We used a focused X-ray beam to scan the phantom at a depth of 5 mm. The focused X-ray beam diameter and the linear scan step size were set to be 100 μm. We used six angular projections with an angular step size of 30 degrees. For each projection, we had 130 measurements. The numerical measurements were generated from the

Biomedical Optics EXPRESS

forward model, in which the phantom was discretized by a finite element mesh with 26,638 nodes, 153,053 tetrahedral elements, and 11,456 face elements. Finally, 1% Gaussian noise was added to the numerical measurements.

2.4 Evaluation criteria

Two criteria were used to evaluate the quality of the reconstructed images, as described in Ref [25].

Center-to-center distance error (CDE): For multiple target imaging, we define CDE as the distance error ratio between the reconstructed targets and the true targets and is given by

$$CDE = \frac{|Dist_r - Dist_t|}{Dist_r} \times 100\% \tag{11}$$

where $Dist_r$ and $Dist_t$ are the CtCD between the reconstructed targets and the true targets, respectively. $Dist_r$ is also calculated from the cross target profile plot using the full width at half maximum (FWHM) approach.

Dice similarity coefficient (DICE): DICE is used for comparing the similarity between the reconstructed and true targets and is given by

$$DICE = \frac{2 \times |ROI_r \cap ROI_t|}{|ROI_r| + |ROI_t|} \times 100\% \tag{12}$$

where ROI_r is the reconstructed region of interest that is defined to be the pixels whose intensities are higher than 20% of the maximum pixel intensity. Generally, the closer DICE is to 100%, the better.

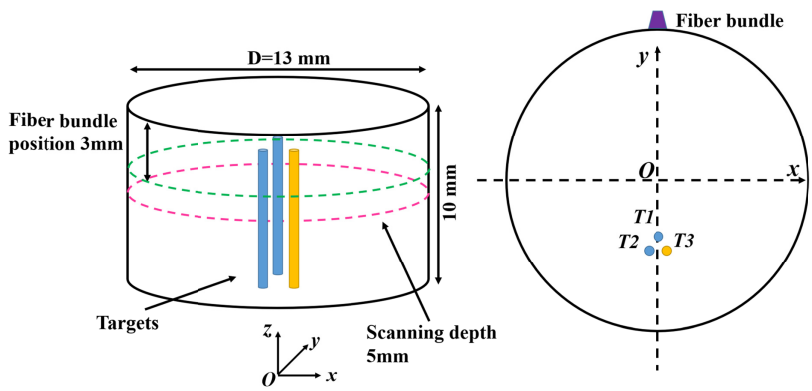

Fig. 2. The phantom geometry and fiber bundle position for numerical simulation with three targets.

3. Result of numerical simulations

The scanned transverse section was discretized with a two-dimensional (2-D) grid having a pixel size of $25 \times 25\,\mu m^2$. The system matrix generated with the finite element mesh was interpolated to the fine 2-D grid. During the reconstruction, the L^1 regularization method was applied using the MM algorithm reconstruction framework to solve the optimization problem. Figure 3 shows the results for numerical simulations of three targets. In Fig. 3(A), the reconstructed time domain XLCT phosphorescence images are plotted. Figure 3(B) shows the zoomed in target region, where the green circles represent the true targets' size and locations. From the reconstructed images, we see that the three targets were reconstructed successfully and have been clearly resolved for phosphorescence yield and lifetime properties,

Biomedical Optics EXPRESS

respectively. To further analyze the reconstructed XLCT image quantitatively, we have calculated the image quality metrics as shown in Table 2. From the dotted blue line in Fig. 3(B), line profiles are plotted in Fig. 3(C). From the FWHM, we calculated reconstructed target size of 0.4249 mm with a target size error (TSE) of 6.23% and 0.4222 mm with a TSE of 5.54% for phosphorescence yield and lifetime, respectively. In addition, the CtCD of yield and lifetime are 0.7769 and 0.7742 mm with errors of 2.89% and 3.23%, and DICE were evaluated to be 89% and 87.62% for yield and lifetime, respectively. Based on our results, the lifetime and yield of multiple targets deeply embedded inside tissues can be successfully reconstructed simultaneously using time resolved data.

To see how robust the proposed time domain XLCT imaging algorithm is to different measurement noises from 1% to 10%, we added different Gaussian white noises onto the numerical measurements and ran the reconstruction with a fixed projection number of 6. We have calculated the image qualify metrics from both the reconstructed lifetime images and yield images as listed in Table 3. Reconstruction using lifetime data with noise levels of 1% and 2% resulted in equivalent CtCD of 0.7769 mm with 2.89% error. At 5% noise level, the CtCD was 0.7755 mm with 3.06% error. At the largest noise level of 10%, the CtCD was evaluated at 0.9515 mm with 18.94% error. DICE coefficients remained larger than 86% in noise levels 1%, 2%, and 5%. For noise level of 10%, the DICE coefficient decreased to 27.53%. The reconstructed yield images resulted in similar DICE coefficients to those utilizing lifetime images, but the lowest DICE coefficient was 85.14% at the greatest noise level. The DICE coefficients at noise levels 1%, 2% and 5% did not fluctuate significantly from 86%. In addition, the lowest CDE of 1.17% occurred at 1% noise level while the greatest CDE of 27.64% occurred at 5% noise level. At noise levels 2% and 10%, CtCD were generated at 0.5844 mm with 26.95% error and 0.6187 mm with 22.66% error respectively.

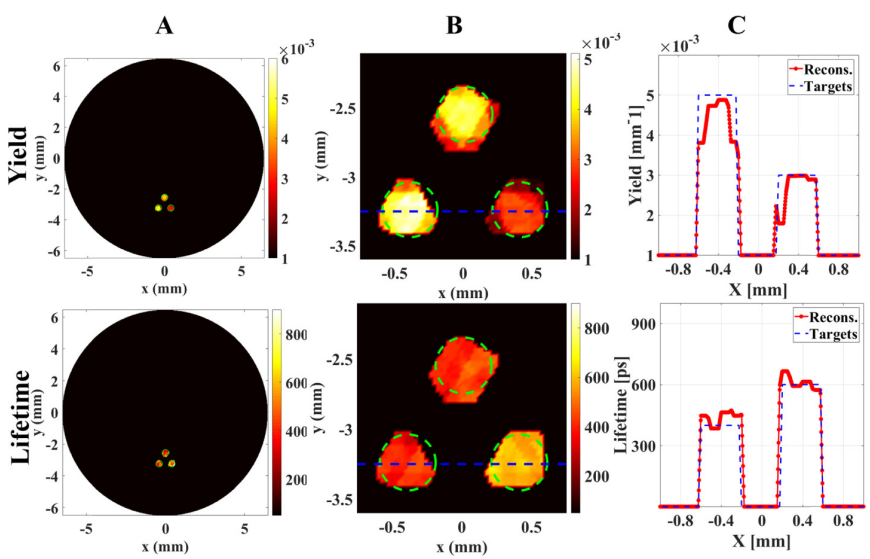

Fig. 3. The reconstruction results of phosphorescence yield (top) and lifetime (bottom) for three targets numerical simulation. A: The reconstructed phosphorescence yield and lifetime images, respectively; B: Zoomed in regions of reconstructed targets, the green dotted line indicates the exact target size and position, the blue dotted line indicates the profile location; C: profile plots across target T2 and target T3.

Additionally, we reconstructed images of lifetime and yield with measurement data at different number of projections with a fixed noise level of 2% as shown in Fig. 4. From these images, we calculated the image quality metrics as listed in Table 4. The reconstructed lifetime images performed best with measurement data of projections 6 and 12 considering

Biomedical Optics EXPRESS

their high DICE coefficients of 87.62% and 86.15% and low CDE of 3.07% and 1.63%, respectively. From the reconstructed yield images, we see that DICE coefficients did not vary significantly with different projection numbers. The greatest DICE coefficient was calculated with 6 projections at 86.32%. The closest CtCD to the actual value was evaluated with 24 projections at 0.8016 mm with 0.20% error, while the greatest CtCD error arose from 3 projections at 1.0560 mm with 32.00% error.

Table 2. Quantitative imaging quality metrics for the numerical simulation with three targets.

	Diameter (mm)/TSE	CtCD (mm)/CDE	DICE
Yield	0.4249/6.23%	0.7906/1.17%	86.49%
Lifetime	0.4222/5.54%	0.7769/2.89%	86.50%

Lastly, we have investigated the robustness of the reconstructed lifetime and yield images to the unknown optical properties. In the forward model, we have set the absorption coefficient of 0.0072 mm^{-1} and the reduced scattering coefficient of 0.72 mm^{-1}. In the reconstruction model, we have changed the optical properties to be 2 times absorption coefficient ($2*\mu_a$), 4 times absorption coefficient ($4*\mu_a$), and 2 times absorption coefficient plus 2 times reduced scattering coefficient ($2*\mu_a$ and $2*\mu_s'$). In these studies, we had a fixed noise level of 2% and a fixed projection number of 6. From both the reconstructed lifetime and yield images, we have calculated the image qualify metrics as listed in Table 5, from which we see that the reconstructed lifetime images seem independent of the optical properties of the object being imaged with the same CtCD of 0.7769 mm with 2.89% error and same DICE coefficient of 86.50%, which are very close to the numbers we got with the true optical properties. From Table 5, we also see that the reconstructed yield images resulted in slightly different metrics with respect to different optical properties. The lowest CDE of 1.52% occurred at $2*\mu_a$ and $2*\mu_s'$ with a CtCD of 0.7879 mm, and the greatest CDE of 27.81% occurred at $2*\mu_a$ with a CtCD of 0.5775 mm. DICE coefficients remained relatively constant at 86% for $2*\mu_a$, and $4*\mu_a$ while the greatest DICE coefficient was generated from $2*\mu_a$ and $2*\mu_s'$ at 87.05%.

Table 3. Quantitative imaging quality metrics for the numerical simulations with different noise levels

	Number of Projections	Noise	CtCD (mm)/CDE	DICE
Lifetime	6	1%	0.7769/2.89%	86.50%
	6	2%	0.7754/3.07%	87.62%
	6	2%	0.7755/3.06%	86.50%
	6	10%	0.9515/18.94%	27.53%
Yield	6	1%	0.7906/1.17%	86.49%
	6	2%	0.5844/26.95%	86.32%
	6	5%	0.5789/27.64%	86.58%
	6	10%	0.6187/22.66%	85.14%

Biomedical Optics EXPRESS

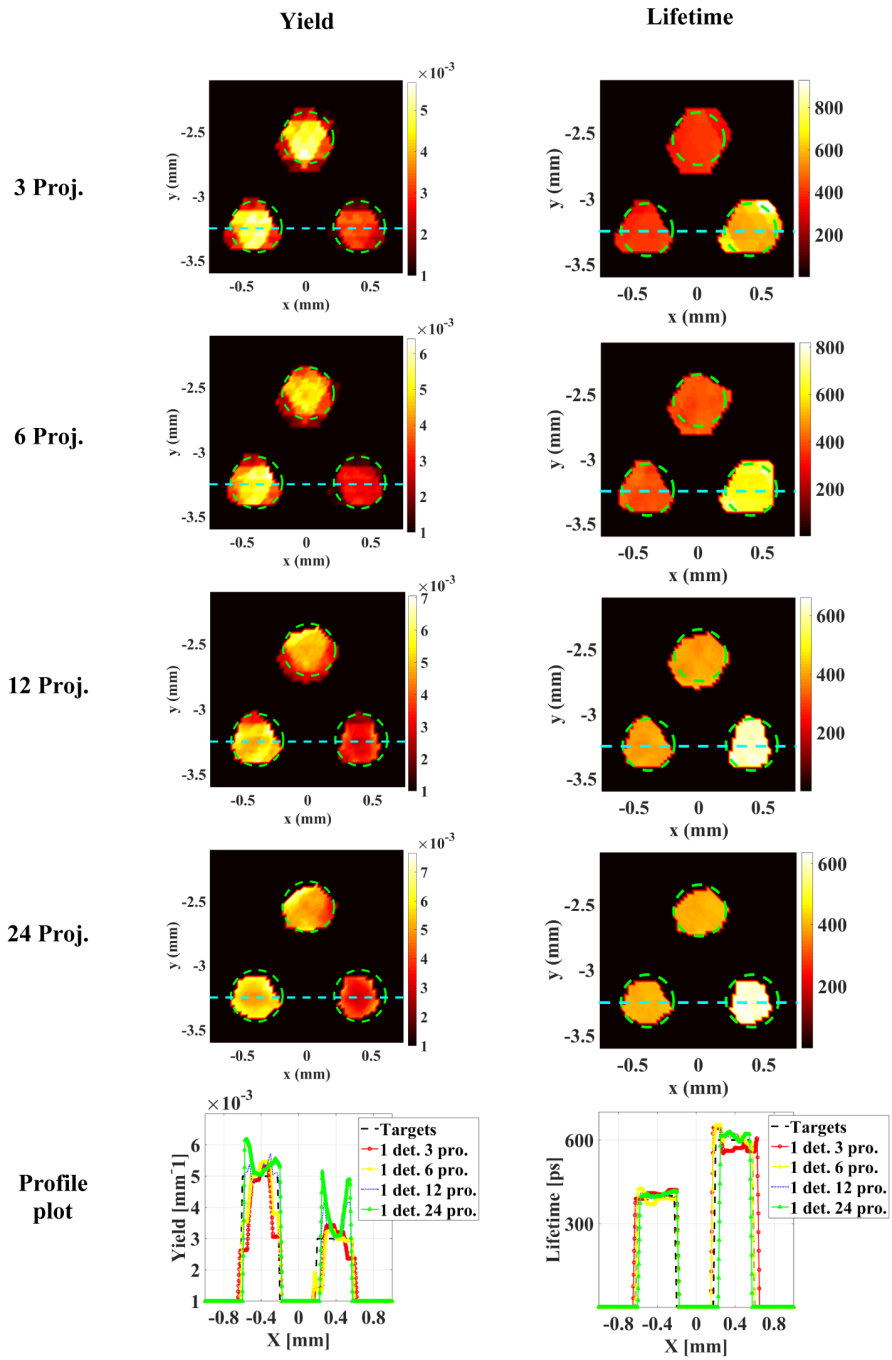

Fig. 4. The zoomed regions of the reconstructed phosphorescence yield images and lifetime images for three targets numerical simulation with measurements at different projections. The dotted circles indicate the true target position and size. The bottom row shows the profile plots cross the bottom two targets where "1 det" indicates one detector we used in the simulations.

Biomedical Optics EXPRESS

Table 4. Quantitative imaging quality metrics for the numerical simulations with measurements of different projection numbers

	Number of Projections	Noise	CtCD (mm)/CDE	DICE
Lifetime	3	2%	0.8113/1.41%	84.32%
	6	2%	0.7754/3.07%	87.62%
	12	2%	0.7870/1.63%	86.15%
	24	2%	0.7878/1.52%	82.41%
Yield	3	2%	1.0560/32.00%	84.36%
	6	2%	0.5844/26.95%	86.32%
	12	2%	0.7906/1.17%	86.16%
	24	2%	0.8016/0.20%	83.35%

Table 5. Quantitative imaging quality metrics for the numerical simulations with mismatched optical properties. The first row indicates the true optical properties with μ_a = 0.0072 mm^{-1} and μ_s' = 0.72 mm^{-1}

	μ_a	μ_s'	CtCD (mm)/CDE	DICE
Lifetime	0.0072 mm^{-1}	0.72 mm^{-1}	0.7754/3.07%	87.62%
	2*0.0072 mm^{-1}	0.72 mm^{-1}	0.7769/2.89%	86.50%
	2*0.0072 mm^{-1}	2*0.72 mm^{-1}	0.7769/2.89%	86.50%
	4*0.0072 mm^{-1}	0.72 mm^{-1}	0.7769/2.89%	86.50%
Yield	0.0072 mm^{-1}	0.72 mm^{-1}	0.5844/26.95%	86.32%
	2*0.0072 mm^{-1}	0.72 mm^{-1}	0.5775/27.81%	86.72%
	2*0.0072 mm^{-1}	2*0.72 mm^{-1}	0.7879/1.52%	87.05%
	4*0.0072 mm^{-1}	0.72 mm^{-1}	0.5789/27.64%	86.39%

4. Discussion and conclusions

In this study, we have, for the first time, proposed a time domain XLCT system design, forward model and reconstruction algorithm. We plan to generate high frequency pulsed X-ray photons by using an optical chopper. The linear GPST method was applied to solve the optical diffusion forward model problem. In three-component target numerical simulations, three targets were successfully reconstructed. Furthermore, phosphorescence yield and lifetime distributions have been recovered simultaneously with good accuracy and resolution. Time domain methods usually take a relatively long scanning time. In the future experimental system, several TCSPC modules can be employed to achieve multiple channel detection to reduce measurement time.

From the numerical simulation studies, we found that the proposed time domain XLCT imaging is robust to measurement noise level up to 5% and to unknown optical properties. In

Biomedical Optics EXPRESS

particular, the reconstructed lifetime images are independent of the optical properties, which is a major advantage of the lifetime imaging due to the difficulty in estimating the optical properties of tissues.

We applied a 20% of maximum threshold when we calculated the DICE coefficient. It is also possible to apply a threshold of 10% of maximum. We have obtained similar DICE coefficients for all cases except the cases with the noise level of 5%. We believe it is feasible to use either 10% or 20% threshold in the future because the measurement noise should be less than 5%.

In this study, we have also used a pair of transform factors as shown in Eq. (8). In the future, more transform factor pairs will be applied from the measured pulses, which should result in better image quality due to more measurement data as input for the reconstruction algorithm.

It is worth noting that the proposed time domain XLCT algorithm is a generic reconstruction algorithm that works for nanophosphors with a lifetime ranging from picoseconds to microseconds. In the numerical simulation studies, we arbitrarily picked up the lifetime of 0.4 and 0.6 nanoseconds, which are enough to validate our algorithm. However, the experimental system as described in Fig. 1 might only work for measuring the lifetime less than hundreds of nanoseconds. For measuring nanophosphors with lifetimes around a few nanoseconds, we need an X-ray source such as free electron laser which can generate X-ray pulses as short as a fraction of nanosecond [26].

We noticed that the DICE dropped slightly when the measurement projection number increased as shown in Table 4. To figure out the reason, we have performed another set of numerical simulations with only one large target (5 mm in diameter) at different projection numbers with a constant noise level. With the large target, we did not observe this issue. A possible explanation is that our tdXLCT reconstruction is based on a finite element mesh and there are partial volume issues due to the small target size. We have also found that the reconstructed image quality could be improved substantially with more detectors instead of one detector as described in our simulations.

The proposed algorithm is a generic reconstruction algorithm that works well for both two-dimensional (2D) imaging and three-dimensional (3D) imaging. Due to the computational cost, we have demonstrated it with a 2D imaging. For 3D imaging, we can scan mice slice by slice of the region of interest.

In summary, we have proposed a time domain XLCT imaging framework and have performed a set of numerical simulation studies to validate its feasibility, which will guide the future design of a time domain XLCT imaging system.

Funding

National Institutes of Health (R01EB026646).

Disclosures

The authors declare that there are no conflicts of interest related to this article.

References

1. G. Pratx, C. M. Carpenter, C. Sun, and L. Xing, "X-ray luminescence computed tomography via selective excitation: a feasibility study," IEEE Trans. Med. Imaging **29**(12), 1992–1999 (2010).
2. M. Lun, W. Zhang, and C. Li, "Sensitivity study of x-ray luminescence computed tomography," Appl. Opt. **56**(11), 3010–3019 (2017).
3. W. Zhang, D. Zhu, M. Lun, and C. Li, "Collimated superfine x-ray beam based x-ray luminescence computed tomography," J. X-ray Sci. and Tech. **25**(6), 945–957 (2017).
4. G. Pratx, C. M. Carpenter, C. Sun, R. P. Rao, and L. Xing, "Tomographic molecular imaging of x-ray-excitable nanoparticles," Opt. Lett. **35**(20), 3345–3347 (2010).
5. C. Li, K. Di, J. Bec, and S. R. Cherry, "X-ray luminescence optical tomography imaging: experimental studies," Opt. Lett. **38**(13), 2339–2341 (2013).

Biomedical Optics EXPRESS

6. D. Chen, S. Zhu, H. Yi, X. Zhang, D. Chen, J. Liang, and J. Tian, "Cone beam x-ray luminescence computed tomography: A feasibility study," Med. Phys. **40**(3), 031111 (2013).
7. W. Zhang, D. Zhu, M. Lun, and C. Li, "Multiple pinhole collimator based X-ray luminescence computed tomography," Biomed. Opt. Express **7**(7), 2506–2523 (2016).
8. W. Zhang, L. Wu, J. Li, X. Yi, X. Wang, Y. Lu, W. Chen, Z. Zhou, L. Zhang, H. Zhao, and F. Gao, "Combined hemoglobin and fluorescence diffuse optical tomography for breast tumor diagnosis: a pilot study on time-domain methodology," Biomed. Opt. Express **4**(2), 331–348 (2013).
9. Y. Zhang, A. A. Khan, G. D. Vigil, and S. S. Howard, "Super-sensitivity multiphoton frequency-domain fluorescence lifetime imaging microscopy," Opt. Express **24**(18), 20862–20867 (2016).
10. L. M. Hirvonen, F. Festy, and K. Suhling, "Wide-field time-correlated single-photon counting (TCSPC) lifetime microscopy with microsecond time resolution," Opt. Lett. **39**(19), 5602–5605 (2014).
11. A. Gibson, J. Hebden, and S. R. Arridge, "Recent advances in diffuse optical tomography," Phys. Med. Biol. **50**(4), R1–R43 (2005).
12. E. Gratton, S. Breusegem, J. D. B. Sutin, Q. Ruan, and N. P. Barry, "Fluorescence lifetime imaging for the two-photon microscope: time-domain and frequency-domain methods," J. Biomed. Opt. **8**(3), 381–390 (2003).
13. S. Liu, Y. Zhang, H. Liang, Z. Chen, Z. Liu, and Q. Zhao, "Time-resolved luminescence imaging of intracellular oxygen levels based on long-lived phosphorescent iridium(III) complex," Opt. Express **24**(14), 15757–15764 (2016).
14. W. Zheng, D. Tu, P. Huang, S. Zhou, Z. Chen, and X. Chen, "Time-resolved luminescent biosensing based on inorganic lanthanide-doped nanoprobes," Chem. Commun. (Camb.) **51**(20), 4129–4143 (2015).
15. K. Hanaoka, K. Kikuchi, S. Kobayashi, and T. Nagano, "Time-resolved long-lived luminescence imaging method employing luminescent lanthanide probes with a new microscopy system," J. Am. Chem. Soc. **129**(44), 13502–13509 (2007).
16. K. Suhling, P. French, and D. Phillips, "Time-resolved fluorescence microscopy," Photochem. Photobiol. Sci. **4**(1), 13–22 (2005).
17. M. Lazarczyk and M. Favre, "Role of Zn^{2+} Ions in Host-Virus Interactions," J. Virol. **82**(23), 11486–11494 (2008).
18. C. Supnet and I. Bezprozvanny, "The dysregulation of intracellular calcium in Alzheimer disease," Cell Calcium **47**(2), 183–189 (2010).
19. H. Lin, P. Herman, and J. Lakowicz, "Fluorescence lifetime-resolved pH imaging of living cells," Cytometry **52A**(2), 77–89 (2003).
20. F. Gao, H. Zhao, Y. Tanikawa, and Y. Yamada, "A linear, featured-data scheme for image reconstruction in time-domain fluorescence molecular tomography," Opt. Express **14**(16), 7109–7124 (2006).
21. C. Li, A. Martinez-Davalos, and S. R. Cherry, "Numerical simulation of x-ray luminescence optical tomography for small-animal imaging," J. Biomed. Opt. **19**(4), 046002 (2014).
22. C. Li, G. Wang, J. Qi, and S. R. Cherry, "Three-dimensional fluorescence optical tomography in small-animal imaging using simultaneous positron-emission-tomography priors," Opt. Lett. **34**(19), 2933–2935 (2009).
23. D. Zhu and C. Li, "Nonuniform update for sparse target recovery in fluorescence molecular tomography accelerated by ordered subsets," Biomed. Opt. Express **5**(12), 4249–4259 (2014).
24. D. Zhu and C. Li, "Nonconvex regularizations in fluorescence molecular tomography for sparsity enhancement," Phys. Med. Biol. **59**(12), 2901–2912 (2014).
25. W. Zhang, M. Lun, A. Nguyen, and C. Li, "X-ray luminescence computed tomography using a focused x-ray beam," J. Biomed. Opt. **22**(11), 116004 (2017).
26. P. Favier, L. Amoudry, K. Cassou, K. Dupraz, A. Martens, H. Monard, and F. Zomer, "The compact x-ray source ThomX," Proc. SPIE **10387**, 1038708 (2017).